Fermilab Library
0 1160 0052538 0

SDC-90-00153

SDC
SOLENOIDAL DETECTOR NOTES

PRE-SHOWER AND SHOWER-MAXIMUM DETECTORS FOR SDC

P. Bonamy, J. Ernwein, P. Le Du, J. R. Hubbard, J. P. Pansart,
G. Apollinari, N. Giokaris, K. Goulianos, P. Melese, R. Rusack, S. White,
G. Bella, J. Grunhaus, R. Heifetz, A. Levy

December 19, 1990

SDC NOTE-90-00153
12-19-90

PRE-SHOWER AND SHOWER-MAXIMUM DETECTORS FOR SDC

P. Bonamy, J. Ernwein, P. Le Du, J.R. Hubbard, and J.P. Pansart
CEN Saclay, France

G. Apollinari, N. Giokaris,
K. Goulianos, P. Melese, R. Rusack, S. White
The Rockefeller University, New York

G. Bella, J. Grunhaus, R. Heifetz, A. Levy
Tel Aviv University, Israel

been taken into account. This degradation will affect the performance of the PS detector more than that of the SM detector, because the PS signals are smaller.

These preliminary GEANT Monte-Carlo studies were performed with just 100 events of each type, so they give only a general impression of the PS and SM detector performances. Further analyses with larger statistics and a more realistic simulation of the SDC detector will be undertaken in the near future.

Isolated Electrons vs. Isolated Charged Pions

Figure 2 shows the clusters of energy produced by electrons and charged pions in a 1 mm thick PS scintillator at $\eta = 0$. Each plot contains 100 events. The simple clustering algorithm used here starts a new cluster if two high bins are separated by at least two low bins. The cluster energy is plotted against the distance between the incident track and the position of the cluster, defined as the position of the fiber with the largest signal. Note that this definition of cluster position gives better position resolution than a center-of-gravity calculation, both in these GEANT studies and in the data of UA2.

For the electrons in Fig. 2a, each track gives a cluster centered within one fiber (1 mm) of the track position, most (96%) with cluster energies larger than 2.4 MeV (15 times minimum ionizing particles). The secondary clusters have smaller energies, and they are at least 3 mm from the incident track (because of the clustering algorithm). The pions in Fig. 2b show a minimum ionizing peak (160 keV) at the track position, containing 71% of the tracks. Most of the other pions interact, producing low-energy clusters at large distances from the incident track.

Identification of isolated electrons requires that there be little energy in the hadronic calorimeter and that the EM calorimeter energy and the momentum measured by the tracking system agree. This identification can be enhanced by a PS detector by requiring at least one cluster that is well-aligned with the incident track (within 1 mm) and which has a large energy deposit (at least 2.4 MeV). These cuts retain 96% of the electrons. For the pions, 21% have clusters which pass the energy cut, but only 5% satisfy the alignment requirement. The pion rejection factor is therefore $96/5 = 19 \pm 9$ ($96/21 = 4.6 \pm 1.1$ without the alignment requirement).

For $\eta = 1.3$, the electron response of the PS detector is degraded for electrons at 40 GeV, as shown in Fig. 3. The energy and position of the cluster closest to the electron axis is shown in Fig. 3a. Cluster positions spread over five 1 mm fibers, and their energies are smaller than those at $\eta = 0$, even though minimum-ionizing signals are twice as big. With an energy cut at 2.4 MeV, only 75% of the electrons are retained, even allowing all clusters within 3 mm of the track position. Furthermore, nearly half of these electrons have large secondary clusters (Fig. 3b).

On the other hand, none of the 100 pions generated had clusters satisfying these cuts ($dE > 2.4$ MeV, $dx < 3$ mm). We can reduce the energy cut all the way down to 800 keV to obtain an electron efficiency of 96%; in this case 8% of the pions are retained for a pion rejection factor of $96/8 = 12 \pm 4$. Thus, high efficiency can be obtained for isolated electrons, with good pion rejection, if secondary electron clusters are allowed.

Note that the PS response at $\eta = 0$ and at $\eta = 1.3$ have been compared for the same electron energy (40 GeV). If instead, we compare electron response at the same p_t, we find that the same cut in cluster energy leads to similar electron efficiency throughout the barrel region. Figure 4 shows the electron response at $\eta = 1.3$ for electrons of 80 GeV ($p_t = 40$ GeV/c). Here 96% of the primary clusters satisfy an energy cut at 2.4 MeV (Fig. 4a).

In the end caps, we have a pure lead PS radiator, and the electron and pion signals are clean, even for electrons of 40 GeV (p_t only 6.7 GeV/c for $\eta = 2.5$). The PS clusters for electrons and pions are shown in Fig. 5. Using strict cuts ($dE > 2.4$ MeV, $dx < 1$ mm), the electron efficiency is 97%, while only 8% of the pions are retained. The pion rejection factor is $97/8 = 12 \pm 4$.

A similar analysis can be applied to the SM detector. Here we assume scintillator elements 2.5 mm thick, with segmentation of 1 cm along the azimuthal direction (roughly 10 segments per tower). At $\eta = 0$, we assume that the SM detector is at a depth of 5.3 radiation lengths (1.3 X_0 from the coil, plus a depth of 4 X_0 in the EM calorimeter). The clustering algorithm still requires two low bins separating distinct clusters. We find that a center-of-gravity measurement of the position of an isolated electron has an uncertainty of 1.1 mm. In this study, we reject electron candidates if the position in the SM detector is off by 5 mm or more. The electron and pion simulations are shown in Fig. 6. We cut at 65 MeV (150 mips) to obtain an electron efficiency of 96%. The corresponding efficiency for pions is 4%. Here the rejection factor of $96/4 = 24 \pm 12$ comes entirely from the energy measurement (the alignment requirement is unnecessary). The SM detector is much less sensitive to junk coming from the coil material. Electron identification at $\eta = 1.3$ is close to that obtained at $\eta = 0$ for the same electron energy.

The pion rejection factors obtained for isolated electrons are similar for the PS and SM detectors defined here (equal, within the limited statistics). This rejection does not depend strongly on the segmentation of the detectors. In particular, we have not used stereo information to obtain these pion rejection factors. On the other hand, this information is undoubtedly highly correlated with the information obtained from the normal analysis of the calorimeter data. We hope to obtain more information on these correlations from test-beam data this spring.

Nonisolated Electrons vs. Neutral Pions Overlapping Charged Pions

The situation is considerably different for nonisolated electrons. Here, a fine segmentation of the PS or SM detector is essential. In the case of a nonisolated electron, we assume that the energy deposit in the hadronic calorimeter tower is contaminated by leak-through from hadrons hitting neighboring towers. We require a single charged track incident on the tower, and an electromagnetic energy deposit equal to the momentum measured in the tracking system (within two standard deviations). We also require that the PS or SM cluster position is aligned with the position of the measured track. We assume that the background comes from neutral pions overlapping with charged pions, and that most of the EM energy comes from the neutral pion. For this reason, we cannot accept candidates which have extra EM clusters which are not aligned with the incident track. We allow neutral pions overlapping spatially with the real electrons as long as the energy deposit agrees with the measured track momentum; the best energy measurement for these nonisolated electrons should come from the tracking system.

At $\eta = 0$, the electron efficiencies are not seriously affected by the rejection of events with secondary clusters. At $\eta = 1.3$, however, the effect is dramatic. Only about 40% of the electrons have a single cluster aligned with the track with energy deposit greater than 2.4 MeV. Further studies will be necessary to evaluate this degradation, which affects principally the PS detector in the region near the ends of the barrel.

Signal and background events in the nonisolated electron study are illustrated in Figs. 7 and 8. In Fig. 8 we see the two types of background which arise from overlapping charged and neutral pions. On one hand, the charged pion can satisfy the electron cuts, while the gammas from the neutral pion convert late and fail to satisfy the energy-deposit requirement. On the other hand, a neutral pion can satisfy the EM energy requirement and overlap the pion track in space. It is this second background which is sensitive to the PS or SM segmentation.

Evaluation of the first background starts from the preceding analysis for isolated electrons, but this time we cannot allow secondary energy clusters. We found that 5% of the charged pions satisfied electron energy and position requirements at $\eta = 0$ in the PS, and 3% in the SM. These charged pion efficiencies are unacceptably large for the case of nonisolated electrons, where the energy in the hadronic calorimeter cannot be used reliably. We reduce this pion background by rejecting electron candidates which have a separate cluster with a large energy deposit that could signal the presence of a neutral pion.

Cluster distributions for 40 GeV gammas and neutral pions at $\eta = 0$ in our PS detector are shown in Fig. 9. Only 86% of the gammas convert in the 2.5

X_0 pre-radiator, and the cluster energies are lower than those of the corresponding electron clusters in Fig. 2a. A cut on the gamma cluster energy at 2.4 MeV removes an additional 24% of the gammas, leaving an efficiency of 62% for single gammas of 40 GeV. For the gammas from the decay of a 40 GeV π^0, the cluster energies are somewhat smaller, as seen in Fig. 9b, and the single gamma efficiency is 56%. The efficiency for detecting at least one of the two photons from a 40 GeV neutral π decay is $[1-(1-0.56)^2] = 81\%$. Background from this source (a large signal from the charged pion and small signals from the neutral pion) is thus estimated to be $0.05 \times (1-0.81) = 1.0\%$ for the PS detector.

In the SM detector, 72% of the 40 GeV gammas have clusters with energies above 65 MeV, as shown in Fig. 10. The same percentage is obtained for each of the gammas from the decay of a 40 GeV π^0. Thus, one of the two photons would be detected for 92% of the neutral pion events. Background is estimated to be $0.03 \times (1-0.92) = 0.24\%$ for the SM detector.

The second background source comes from the overlap of the converted gammas with the incident charged-pion track. Here the stereo information from the PS or SM detector has an important role to play. With a PS stereo angle of 30 degrees, the position uncertainty along the beam direction is about twice its azimuthal value. At $\eta = 0$, we reject events with clusters in the PS more than 2 mm from the track azimuthally, or more than 4 mm from the track along the beam. This gives a geometrical acceptance of 0.3% for a 100×100 mm^2 tower. The combined acceptance for a charged pion plus a neutral pion in the same tower would then be 1.3%. The electron efficiency, after rejecting candidates with secondary clusters, is 95%, so the pion rejection factor is $95/1.3 = 73 \pm 28$. However, we have not yet taken account of possible ghosts arising in our long (2 m) PS fibers.

For the SM detector discussed above, with 10 azimuthal segments per tower and a position resolution of 1.1 mm, the geometrical acceptance would be 6% (accepting clusters within 3 mm of the track). This geometrical acceptance would dominate the other background source, and the combined rejection factor would be only $96/6 = 16 \pm 1$. Using crossed SM segments (2×10 segments per tower) would reduce the geometrical acceptance to 0.36%; the combined acceptance would then be 0.6%, and the rejection factor 160 ± 36.

Isolated Gammas vs. Isolated Neutral Pions

The efficiency for observing isolated gammas is higher than the gamma efficiency discussed above, because it is not necessary to observe a gamma signal in the PS or SM detector to identify an isolated gamma. Only candidates with two showers visible in a PS or SM detector are removed. In the case of a SM detector,

a candidate may also be rejected because the spatial extent of the shower is larger than expected for a single gamma.

For isolated gammas, there are no tracks incident on the calorimeter towers in question. The best rejection for neutral pions is obtained by setting the cluster-energy cut at a low value. For a PS detector at $\eta = 0$, 14% of the single gammas at 40 GeV fail to convert in 2.5 radiation lengths and another 9% have clusters below a cut at 800 keV, 62% have at a single cluster greater than 800 keV, and 15% have more than one such cluster (see Fig. 9). The gamma efficiency (zero or one clusters) would be 85%. The detection efficiency for each gamma from a 40 GeV π^0 decay (one or more clusters above 800 keV) is 74% (see Fig. 9b). The probability of a 40 GeV neutral pion passing the isolated gamma cuts is about 34%, so the rejection factor against neutral pions is $85/34 = 2.5 \pm 0.5$.

This rejection factor assumes that the two gammas from the π^0 decay can be observed separately in the PS detector. We should obtain efficient separation if at least 3 low bins separate the two cluster peaks. This requires a separation of about 4 mm in azimuth or 8 mm along the beam direction. Here, we require separation in two of the three PS stereo views, so the distance between gammas must be greater than about 6 mm. At $\eta = 0$, the minimum distance between the two gammas from a π^0 decay is $R*(0.270\ \mathrm{GeV})/E(\mathrm{GeV})$, so we should be able to reject neutral pions with energies below 90 GeV.

For the endcap PS detector, the stereo angle is larger (45 degrees), and we should be able to separate gammas down to distances of about 4 mm. Furthermore, the distance from the intersection point to the PS is about twice as big as it is at $\eta = 0$. Therefore, we should be able to reject neutral pions in the endcaps with energies up to about 270 GeV.

For an SM detector at 5.3 X_0, 98% of the gammas convert. We can set a cluster-energy cut at 8.8 MeV, so that none of the gammas give more than one cluster (see Fig. 10). The gamma efficiency is then 95% even if we require a cluster above the energy cut (100% if only multiple clusters are rejected). Of the neutral pions, 10% would be retained by this cut, giving a rejection factor of 10 ± 3.

This time the distance between the two gammas must be sufficiently large to significantly increase the width of the SM signal. The Moliere radius of the EM shower is 1.2 cm, so the minimum distance between the two gammas is probably about 2 or 3 cm (assuming 2×10 segments per tower). At $\eta = 0$, this corresponds to a maximum π^0 energy of 27 or 18 GeV, respectively. At $\eta = 2.5$, we could reject neutral pions up to about 70 GeV with this SM detector.

Future Simulation R&D

The above analysis provides a general view of the performance of the PS and

SM detectors, but much work still needs to be done. The GEANT Monte Carlo simulations discussed above will be run with higher statistics and with a better detector geometry. Realistic angular and energy distributions will be used and more advanced algorithms for selecting clusters will be explored. Bremsstrahlung, gamma conversions, particle interactions in the inner detector, and neutron albedo from the calorimeter will be considered. Furthermore, the effect of multiple interactions at possible SSC luminosities will be studied.

PHYSICS EVALUATION

We have used PYTHIA to generate events for certain physics processes chosen for the evaluation of PS and SM performance. We have studied processes invoked in the PAC questions, by preference. These events have not been run through GEANT. In particular, bremsstrahlung and gamma conversions in the detector material before the PS detector have been ignored. The effect of the magnetic field on particle trajectories has been included.

For isolated electrons, we felt that the information from the matching of the calorimeter energy and the momentum measured in the tracking system (E/p) should be sufficient to provide clean signals in the barrel region, where the full magnetic field is available. On the other hand, we felt that additional information might be necessary in the forward direction, because the magnetic field integral falls off as the square of the radius. The physics process chosen was Higgs decay to four leptons.

For nonisolated electrons, we studied top decays into a W plus a b quark, where the b quark decays semi-leptonically into a charm quark, an electron, and a neutrino. Nonisolated muons play an important role in our planned analysis of top decays, and these analyses would be more convincing if we had the redundancy provided by the analysis of nonisolated electrons.

For the isolated gammas, we chose the associated production of a Higgs and a W, followed by Higgs decay into two gammas.

Higgs Decays Into Four Leptons ($H \rightarrow e^+e^-e^+e^-$)

In the Standard Model, the best channel for the Higgs search is the decay mode $H \rightarrow ZZ$. For Higgs masses above the ZZ threshold (and up to about 600 GeV), we are not limited by statistics, and Z decays into electron and muon pairs give clear signals for the Higgs. In this Higgs mass region, the mass constraint on the Z is sufficient to confirm the identity of the electrons. The situation is different for Higgs masses below the ZZ threshold. The number of events is more

limited (insufficient for discovery for Higgs masses below 120 GeV), and the Z mass constraint applies to only one of the lepton pairs. Additional identification could be important for the electrons from the Z^* decay, especially in the forward direction if E/p matching is weakened because of the smaller effective magnetic field.

We have calculated the uncertainty in E/p for the electrons from $H \to ZZ^*$ using the simulation parameters from Chapter 5 of the SDC EoI. In Fig. 11, we plot this uncertainty as a function of the pseudorapidity (η), for electrons from $Z^* \to e^+e^-$ and for $Z \to e^+e^-$, for decays of a Higgs of mass 120 GeV. We see that the mismatch in E/p is less than 10% for the electrons from the Z^* decay, and that the uncertainty is smaller in the forward region ($1.5 < \eta < 2.5$). In fact, $\sigma(p)/p = \sigma(p_t)/p_t$ is small at all η because p_t is small for these Z^* decays. On the other hand, $\sigma(E)/E$ is large in the central region because the electron energy is small; in the forward region, E is larger, and $\sigma(E)/E$ scales as $1/\sqrt{E}$. Our conclusion is that there is no special requirement for extra electron identification in the forward region for the $H \to ZZ^*$ analysis.

We have repeated this analysis for the decay $H \to ZZ$ above the ZZ threshold. The uncertainty in E/p is shown in Fig. 12 for electrons from Higgs decays with Higgs masses of 200 and 800 GeV. The uncertainties are small for the 200 GeV Higgs, but they become large for the 800 GeV Higgs, especially in the forward direction. Here, extra identification power could be useful, although the Z mass constraint can still help in identifying the electrons. Our conclusion is that the identification of isolated electrons from $H \to ZZ$ events is not a compelling reason for a PS or SM detector in SDC.

Top Decay to Nonisolated Electrons ($t \to W + b \to \mu\nu + ce\nu$)

We generate pairs of top quarks with a top mass of 250 GeV. We selected top decays into a b quark and a W boson, followed by b decay into a c quark, an electron and a neutrino, and W decay into a muon and a neutrino. The muon from the W decay is required to have $p_t > 40$ GeV/c. The electron from the b decay is required to have $p_t > 15$ GeV/c. The solenoidal magnetic field is taken to be constant, with $B_z = 2$ Tesla.

We look at the calorimeter tower containing the electron from the b decay. We find that 73% of the electrons are alone in their calorimeter tower, 24% have a neutral pion directed toward the same tower, and 6% have a charged pion in the same tower (3% have both charged and neutral pions in the same tower). The average particle energies are 35 GeV for the electron, 20 GeV for the neutral pions, and 50 GeV for the charged pions. The lower-energy charged pions are swept away

by the magnetic field. Figure 13 shows the sums of energies of neutral and charged tracks entering the tower containing the electron.

Our algorithm for identification of nonisolated electrons would retain most of the electrons which are alone in their calorimeter towers (except for a PS at $\eta = 1.3$, where as few as 40% of the electrons would be retained, as discussed above). The algorithm would reject electrons with a charged pion in the same tower, and it would reject about half of the electrons with a neutral pion in the same tower. (These are mostly low-energy π^0's, as shown in Fig. 13a, with a peak near 5 GeV, so the two gammas will often hit two different calorimeter towers.) The final efficiency for these electrons from the decay chain $t \rightarrow b \rightarrow e$ would be about 85%. Background events with overlapping neutral and charged pions should be reduced by about two orders of magnitude by a PS or by a SM with crossed segments in each tower.

Higgs Decay Into Gamma Pairs ($W + H \rightarrow \mu\nu + \gamma\gamma$)

We have generated events with the associated production of W and Higgs bosons, followed by W decay to a lepton and a neutrino, and Higgs decay to a gamma pair. This Higgs decay mode gives the best chance for Higgs discovery if the Higgs mass is close to the mass of the Z (the Z cannot decay into gamma pairs). Associated production of the Higgs with a W boson was chosen because the resolution of the SDC calorimeter is insufficient to permit discovery of the Higgs above the background of QCD gamma pairs. Unfortunately, there are few events in this mode, and several standard SSC years might be required to observe the signal.

Signal events were required to have $p_t > 20$ GeV/c for the lepton from the W decay and for each of the gammas from the Higgs decay. Backgrounds to this small signal arise from $W + \gamma\gamma$, $W + \gamma$+jet, and W+ jet jet events, where the jets in question fragment so as to look like isolated gammas. The PS or SM can do nothing to reduce the direct gamma background, but it can remove background from jets which fragment to one or more neutral pion. In fact, as shown in the SDC LoI, somewhat less than half of the background is due to the irreducible $W + \gamma\gamma$ background, and most of the rest comes from $W + \gamma$ + jet events[1]. (Note that the probability of a jet faking a gamma was estimated from CDF data to be 5/10000. This estimate could be wrong by an appreciable factor.)

In order to investigate the ability of a PS or SM detector to remove the single π^0 background to this Higgs signal, we have plotted in Fig. 14a the gamma energy as a function of η for the $H \rightarrow \gamma\gamma$ events, for a Higgs of mass 120 GeV. In Fig. 14b, we show the minimum distance between the two gammas from a π^0 decay for a π^0 with the same energy and the same direction as each of the gammas in Fig. 14a.

Detection limits in the PS barrel and endcaps and in the SM are indicated, as discussed above (6 mm in the PS barrel, 4 mm in the PS endcaps, and 30 mm in the SM detectors). We see that most of the gammas have energies which allow background reduction using a PS detector, but that a SM detector is of no use for this analysis.

The rejection factor that can be obtained with the PS detector is about a factor two, so we would expect to remove about one-fourth of the background under the Higgs signal. If the jet background is larger than expected, the PS detector could be expected to remove half of this larger background.

Future Improvements

We will improve the physics simulations discussed above, and extend them to other physics processes. Backgrounds due to the underlying event and to luminosity-dependent multiple interactions will be evaluated. Reconstruction and trigger algorithms will be developed, and the algorithms for the identification of electrons in jets and isolated gammas will be improved. GEANT will be used to obtain realistic event simulation in the SDC detector environment and to investigate the most desirable configuration of the PS/SM detectors and their optimum location in the SDC detector. Physics simulation and algorithm development will be carried out at Saclay, Tel Aviv, and Rockefeller University.

MECHANICAL DESIGN

The design considerations are quite different whether one considers a PS or a SM detector. A PS detector is a separate piece of equipment which will be placed in the space between the magnet coil and the EM calorimeter in the barrel region, and in front of each end cap calorimeter. The SM detector, on the other hand, is an integral part of the EM calorimeter.

Pre-shower Design

A preliminary design of a full scale PS detector for the SDC has been made, using the original EoI parameters (see Fig. 15). The detector is made of a converter followed by three double layers of staggered scintillating fibers, 1 mm in diameter. The center-to-center spacing of the fibers in each layer is 1.5 mm, so the effective spacing in each double layer is 0.75 mm. The three double layers are arranged into stereo views. Layers of fibers are imbedded in extruded plastic grooves supported by honeycomb panels which provide the structural strength. Clear fibers bring the light out through the crack at $\eta = 1.5$ to the space behind the calorimeter where the optical detectors and the front-end electronics are located.

In the barrel region (Fig. 16), the converter material consists of the magnet coil plus a lead sheet whose thickness decreases along the beam axis so that the amount of material seen by a particle from the interaction zone is constant at 2.5 radiation lengths. In this region, the fibers run in the axial direction, or at stereo angles to the axial direction. The total space needed to install the barrel PS detector between the coil and the calorimeter is 9.5 cm. The PS detector is made of 4 m×1 m elements which are assembled around the coil before it is inserted into the calorimeter.

The endcap PS detectors (Fig. 17) use fibers with the same spacing as in the barrel region arranged in three views in a plane perpendicular to the beam axis. They are placed behind a lead sheet with a constant thickness of 2.5 radiation lengths. Each endcap PS detector is delivered in one preassembled piece.

In the descoped version of the PS detector appropriate to the LoI, the main features of this design are unchanged, but the fiber diameter is 1.5 mm, and the effective spacing in each double layer is 1.0 mm. The number of fibers is 140,000 in the barrel and 20,000 in each endcap detector. A preliminary schedule calls for four years to design, prototype, test, and build the PS detectors, and two months for installation. Table 1 shows some of the design parameters for the descoped PS detector.

Table 1. Pre-shower Detector Design Parameters

Fiber diameter, length	1.5 mm, 2 m
Number of fibers :	140,000 (barrel) 20,000 (each end cap)
Total weight (tons)	8 (coil+lead in barrel) 3.4 (end cap)
Radiation lengths (lead + coil)	2.5
Radiation lengths (PS detector)	0.05-0.12

Shower Maximum Detector

Because the SM detector is imbedded in the EM calorimeter, the design will be very dependent on the technique used for the calorimetry. In the case of scintillating tiles read out by WLS fibers, a SM tile could be divided into 8 parallel strips, each $\sim$ 1.5 cm wide. Two such SM tiles could be located $\sim$ 5 and 6 radiation lengths deep in the electromagnetic calorimeter tower with strips running in perpendicular

directions. The Monte Carlo simulations described above show that nonisolated electrons are more easily separated from $\pi^{\pm}\pi^{0}$ background when a SM detector with crossed strips is used.

The only constraint on the mechanical design of the electromagnetic tower in the tile/fiber option is that additional fibers must be brought to the back of the calorimeter. The design must provide paths for fibers from the perpendicular strips of the SM tiles.

READOUT OPTIONS

A primary issue which concerns all those interested in fiber PS/SM detectors at the SSC is the readout. Such a system must be able, at reasonable cost, to:

1. Provide pulse-height information for individual fibers;
2. Distinguish between events every 16 ns;
3. Supply simple information sufficiently rapidly to participate in a 1st level trigger;
4. Store the events for several μs (until the first level trigger decision);
5. Readout selected events at KHz rates;
6. Operate in the presence of stray magnetic fields;
7. Survive for several years at SSC radiation levels; and
8. Complement the calorimeter without compromising its hermiticity.

Since PS/SM detectors sample the electromagnetic shower, the number of photons per fiber is much larger than the number available in fiber tracking. The PS/SM detectors need not be sensitive to minimum ionizing particles, although this would be desirable. The segmentation required of a PS/SM detector is finer than that of the calorimeter, and the light output is less, so more channels are required, with greater sensitivity; on the other hand, the linearity requirements can be relaxed. Earlier fiber pre-shower detectors used a CCD plus image intensifier chain, which was well matched to the light output and granularity of such devices, but this read-out system is too slow (5 ms) for SSC operation.

We plan to examine the feasibility and to compare the relative advantages of three types of readout systems for PS/SM detectors: Position Sensitive Photomultiplier tubes (PSPMT), Avalanche Photodiodes (APD), and Image tubes with a LBL "smart pixel" detector at the anode (PIXIES).

Position Sensitive Photomultipliers Tubes

PSPMT's with crossed wire readout now exist at a cost of $10 per channel

and require 34 ADC channels to readout 228 fibers. This is a relatively recent development in photomultiplier technology and it is to be expected that this type of readout could become more cost effective in the near future. Pulse height sharing can give good position resolution, but this projective readout technique is subject to ghosts in high-occupancy environments. There is a possibility of adding an additional cross grid to resolve ambiguities; this possibility will have to be explored in collaboration with industry.

Avalanche Photo-Diodes

APD's have a different spectral response than conventional photo-cathodes and a larger quantum efficiency. General Electric now has APD's with sufficient gain to make them interesting for PS/SM detectors, even though they may be marginal for tracking systems. Further development is necessary to improve their pulse-height information. Economic sparse readout of the APD's must be developed.

Saclay and Northeastern University, in conjunction with GE of Canada, are evaluating APD's for PS and SM detectors. Preliminary tests shows that they are already suitable for SM detectors, where the light output is not a problem. A compact readout chip integrating 16 to 32 channels of APD's, low noise amplifiers, and analog two-microsecond pipelines is under evaluation.

Pixel Image Tubes

Pixel Image Tubes (PIXIES) are another development which could provide an economic readout for PS/SM detectors. These are conventional proximity focussed image tubes which use the LBL pixel detector[2], to detect the accelerated photo-electrons at the anode. This pixel detector is being developed for use in the SDC central tracker.

An outline of a possible PIXIES device is shown in Fig. 18. It would consist of a fiber-optic window with a conventional photo-cathode. The image at the photo-cathode is projected onto a silicon anode which consists of a pixel array with SMART readout. The amplification is achieved by applying a voltage of 10 kV between the photo-cathode and the anode, giving a signal of 2,000 to 3,000 electron-hole pairs per photoelectron, with an input noise equivalent to 100–200 electrons. The particular advantage of pixel image tubes is that they can read out up to 400 1 mm diameter fibers per channel.

Occupancy considerations must play a role in choosing the PS/SM detector configuration used in conjunction with PIXIES to prevent saturation of the SMART readout. For minimum bias events, the occupancy of a 2.5 m long, 1 mm diameter fiber located at a radius of 2 m is 0.5%, for a luminosity of 10^{33} $cm^{-2}s^{-1}$.

Hamamatsu, DEP and Burle have expressed interest in developing devices of this kind with an expected final production cost of about $5000 per tube. These proposals have been supplied to the SSC Lab by the sub-system group. All three companies have commented on the possible commercial interest of this device. Partial funding for PIXIES R&D has been requested from the Texas Commission.

Summary of Readout Options

Several factors enter into the choice of readout to be selected for PS/SM detectors, including cost, simplicity, and compatibility with the rest of the SDC detector. Some aspects of the different readout options under investigation are summarized in Table 2.

Table 2. Comparison of PS/SM Readout Options

SYSTEM	FIBERS/ADC	COST/FIBER ($)	COMMENTS
PSPMT (wire anodes)	10	10	x-y readout with ghosts
APD	1	?	High gain amplifier required
PIXIES	$\sim$ 500	$\sim$ 10	Readout saturates at high occupancy

TRIGGER DESIGN

Pre-shower and shower maximum detectors can provide useful information to the trigger at Level 2 by providing pulse-height information matched to the tracker and locally matched with clusters in the calorimeter. A possible trigger would require a track pointing to a pre-shower cluster in conjunction with a cluster in the calorimeter. Local matching, without reference to a central trigger system, between the clusters in the preradiator and energy deposition in the calorimeter can help remove spurious triggers from the electron trigger at Level 1. Experience in OPAL has indicated that triggers formed with the tracker, the calorimeter, and the preradiator are best combined as three separate pairs instead of one triplet. This provides a very useful degree of redundancy. Furthermore, if the preradiator can indicate the presence of a π^0 through fine spatial segmentation, then the purity of the electron trigger can be improved.

Possible methods for incorporating PS/SM detector information in the Level 2 trigger are being evaluated at Saclay. One possibility being studied is the combination of PS/SM data with that of the tracking and calorimeter systems using massive parallel processing (MPP) devices. An evaluation obtained with a trigger

simulator shows that decisions such as electron isolation and missing E_t could be available 10 to 30 microseconds after the beam crossing.

PROTOTYPE CONSTRUCTION AND FUTURE BEAM TESTS

We are building a modular prototype PS/SM detector system to be tested in conjunction with a tile-fiber calorimeter this coming spring in a Fermilab test beam. The purpose of these tests will be to study the correlations between the response of the PS and SM detectors and that of the calorimeter. This will be done with particular emphasis on the e/π separation, in a realistic configuration.

The PS test module will consist of two planes of fibers each consisting of 3 stereo views, each view composed of two layers of 1 mm fibers with 1.3 mm fiber-to-fiber spacing. The two fiber planes will be placed at depths between 2 and 3 radiation lengths. The fibers will be readout with an image intensifier system similar to that used in the Yale/Rockefeller beam tests. This PS test module is under construction at Rockefeller University.

The SM test array will consist of 1-cm strips, readout by WLS fibers. It will be placed at a depth of 5 or 6 radiation lengths in the EM calorimeter. This array is being built by ANL for the tile-fiber calorimeter sub-system group.

RADIATION DAMAGE STUDIES

A major effort to improve the radiation hardness of scintillating fibers is under way in many laboratories. For fibers used in the PS detector, radiation damage will not be much worse than for fibers used in the tracking detector. There is added activity due to conversions in the coil and in the lead converter, but the PS detector is located at a larger distance from the interaction point. On the other hand, a SM detector will be exposed to the highest radiation doses in the detector. For both PS and SM detectors, the photo-detectors and front-end electronics are located behind the calorimeter, and are thus protected from high radiation doses.

We are engaged in a program designed to study the radiation hardness of a scintillator EM calorimeter module in a 2 GeV electron beam at Orsay. The first stage, consisting of exposure of various scintillating tiles and fibers to a Cobalt source, has already begun. This will allow us to choose the best available material for building a prototype EM calorimeter module. By monitoring the response of this module, and, in particular, of tiles located at shower maximum, during several months of exposure to radiation from the electron beam, we hope to determine the maximum dose compatible with acceptable calorimeter performance. The results

of these study will tell us in which region of η the scintillator EM calorimeter can be used without suffering unacceptable radiation damage.

REFERENCES

1. M. Mangano, "Production of $WH \rightarrow W\gamma\gamma \rightarrow e\mu\gamma\gamma$," Solenoidal Detector Collaboration Note SDC-90-00113 (1990).
2. D. Nygren, "Silicon Tracking Devices for the SSC", in the *Proceedings of the Summer Study on High Energy Physics in the 1990's*, (July 1988).

Preshower

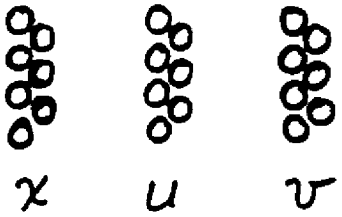

1.5 mm fibers
1.0 mm step
Stereo ± 30° ?

$\eta = 0$ 1.3 X_0 Al + 1.2 X_0 Pb
$\eta = 1.3$ 2.6 X_0 Al
$\eta = 2.5$ 2.5 X_0 Pb

R = 2 m 4 × 2 m

Barrel : 140 k channels
Ends : 40 k channels

Shower Max

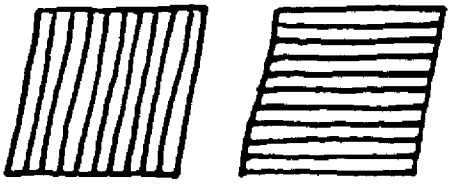

2 × 10 channels / tower

Barrel : 154 k channels
Ends : 60 k channels

Figure 1 .
Model PS and SM detectors.

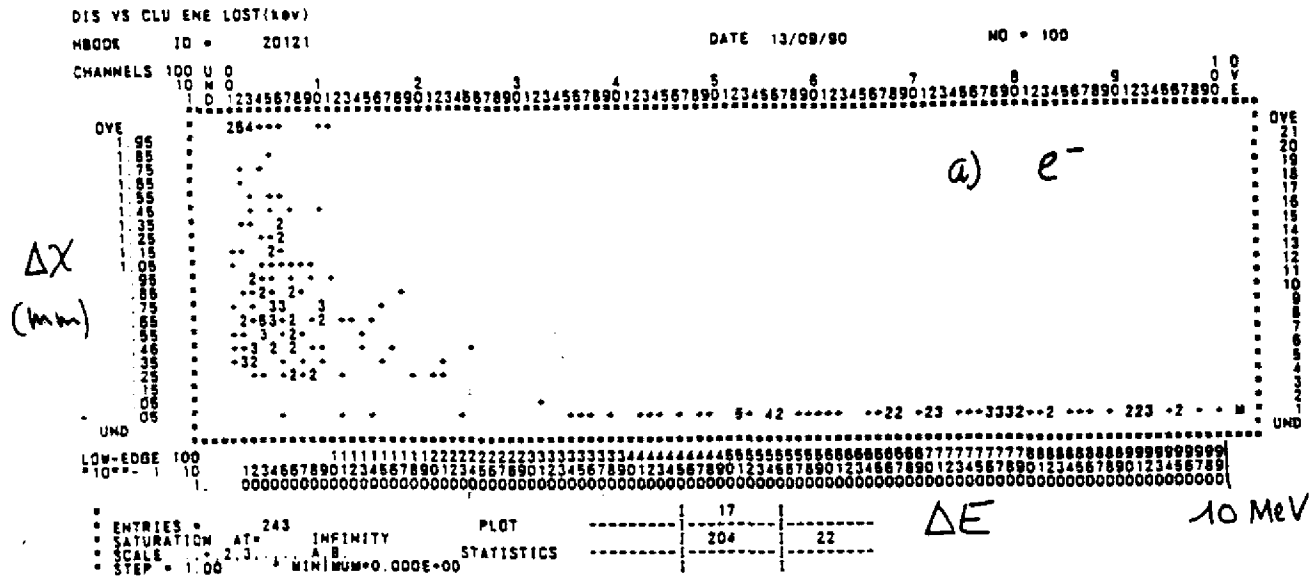

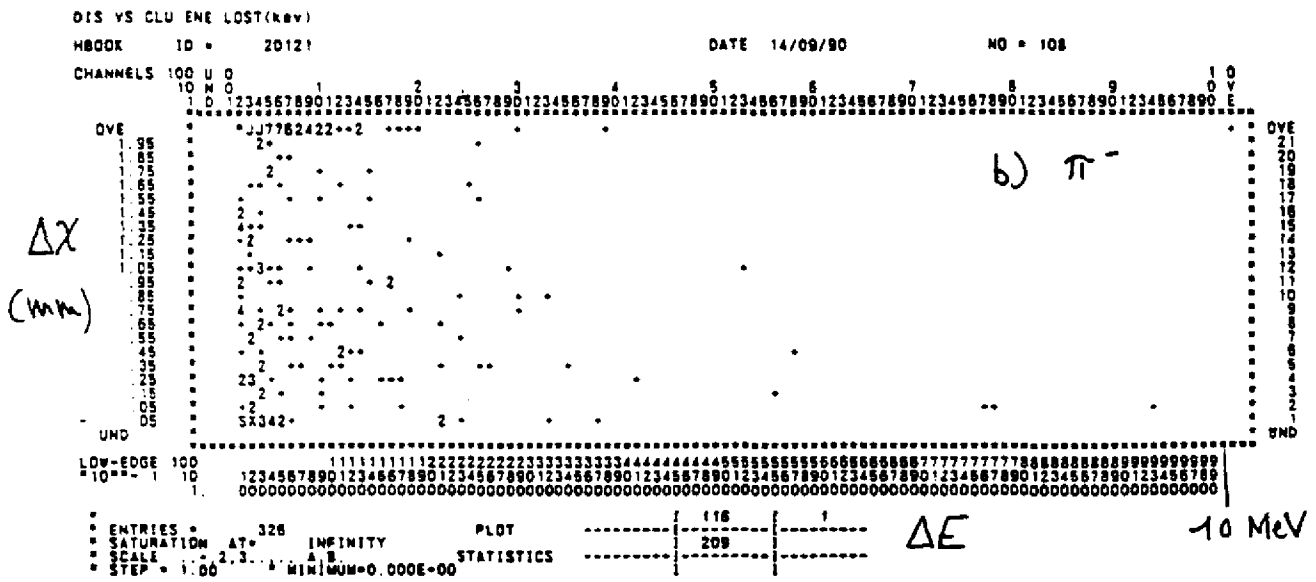

Figure 2.

Clusters in a PS detector at η=0.

a) Electrons with E= 40 GeV, 100 events.

b) Charged pions with E=40 GeV, 100 events.

Cluster energy is plotted against the distance from the incident track (in mm).

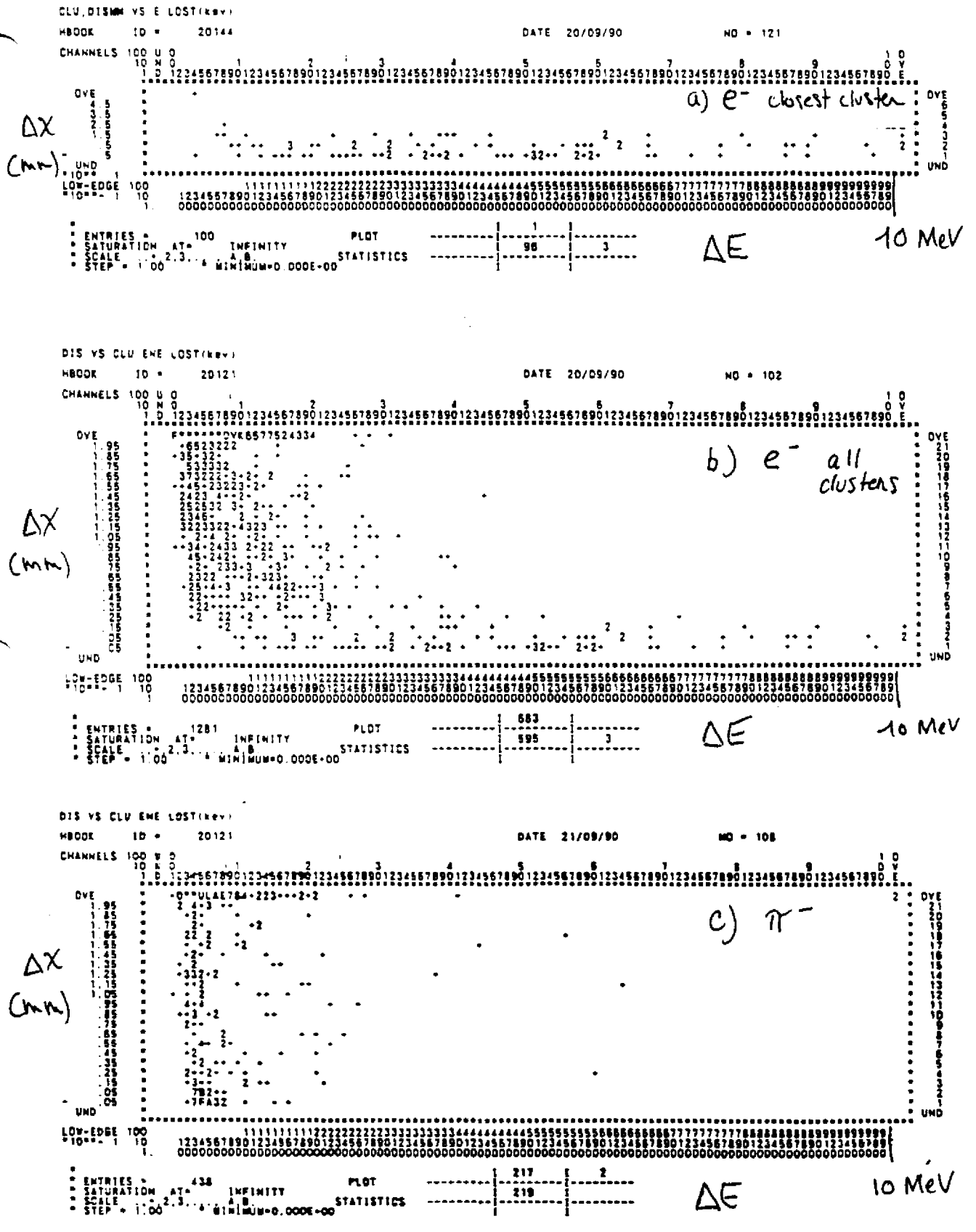

Figure 3.

Clusters in a PS detector at $|\eta| = 1.3$, E=40 GeV.

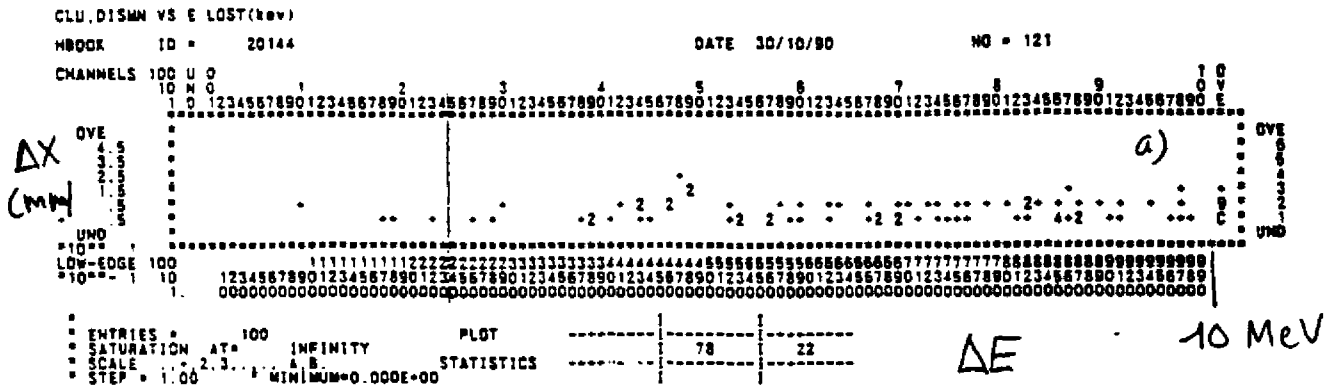

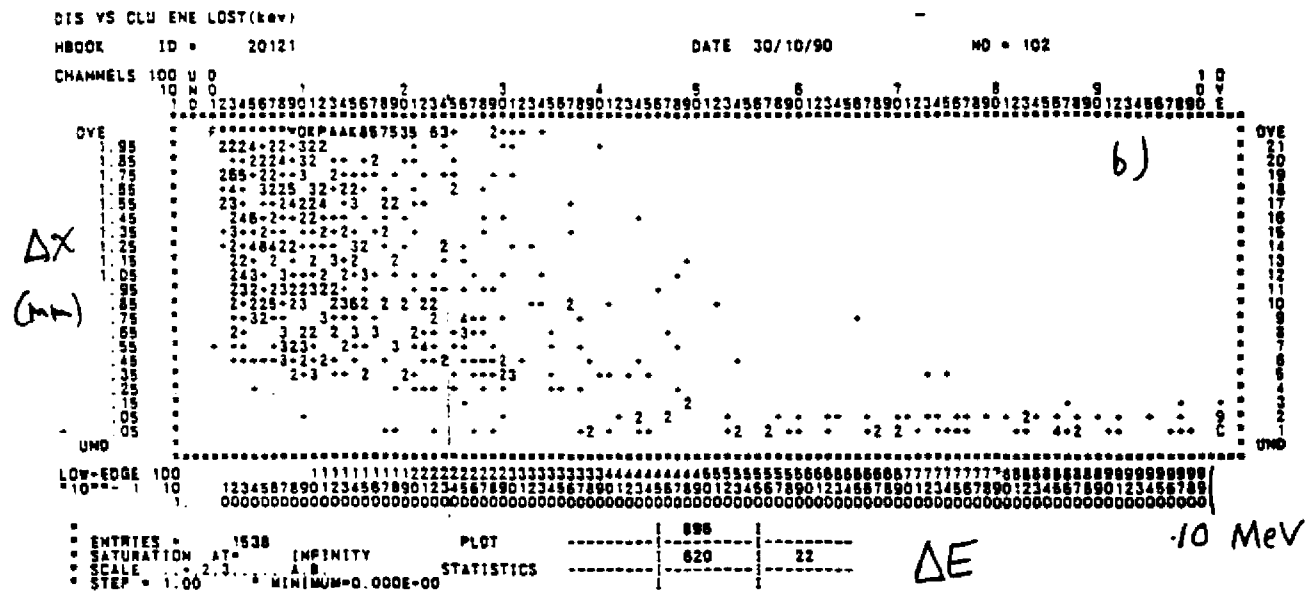

Figure 4.

Electrons in a PS detector at $|\eta| = 1.3$, E=80 GeV (E_t=40 GeV).

a) Closest cluster.

b) All clusters.

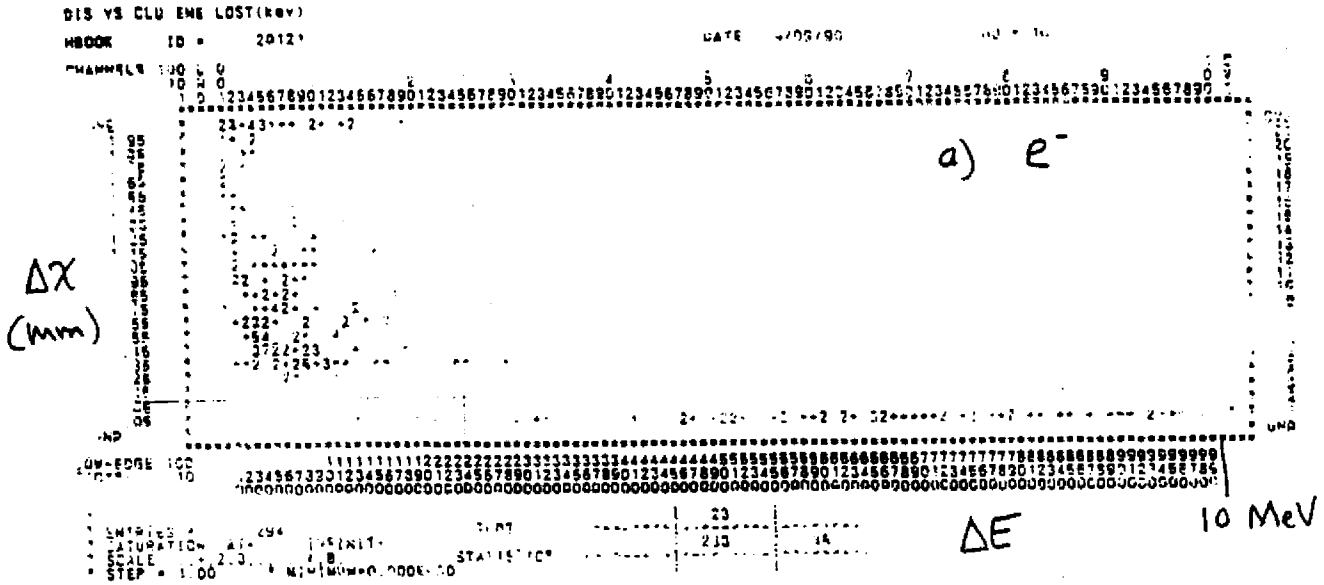

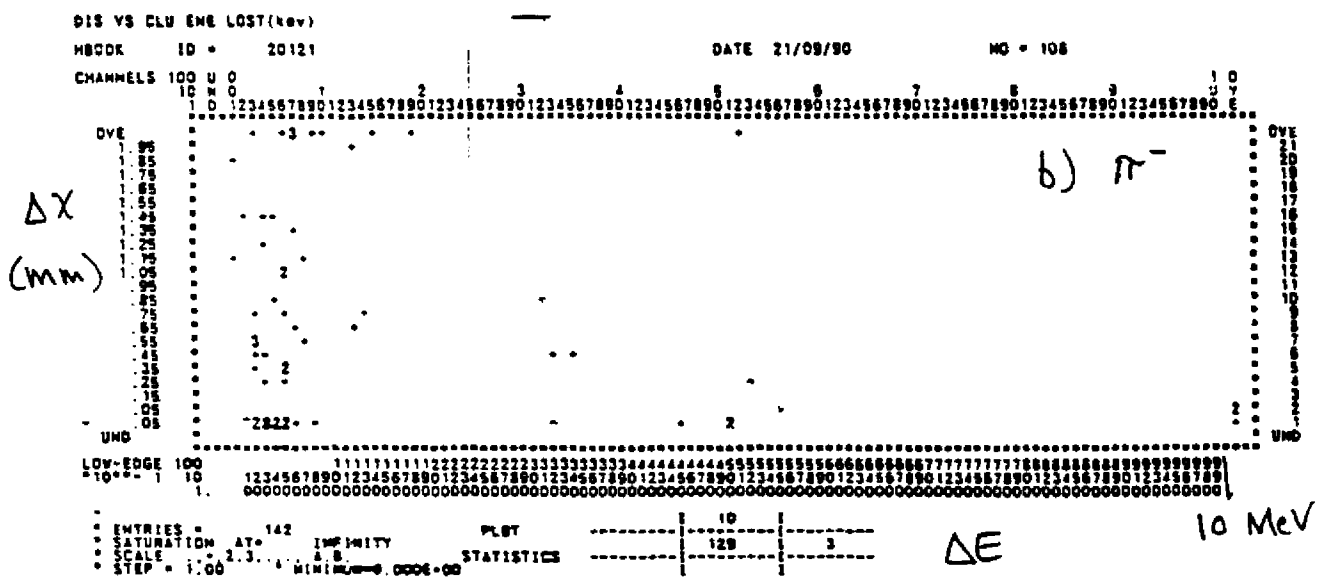

Figure 5.

Electrons in a PS detector at $|\eta| = 2.5$.

a) Electrons with E=40 GeV.

b) Charged pions with E=40 GeV.

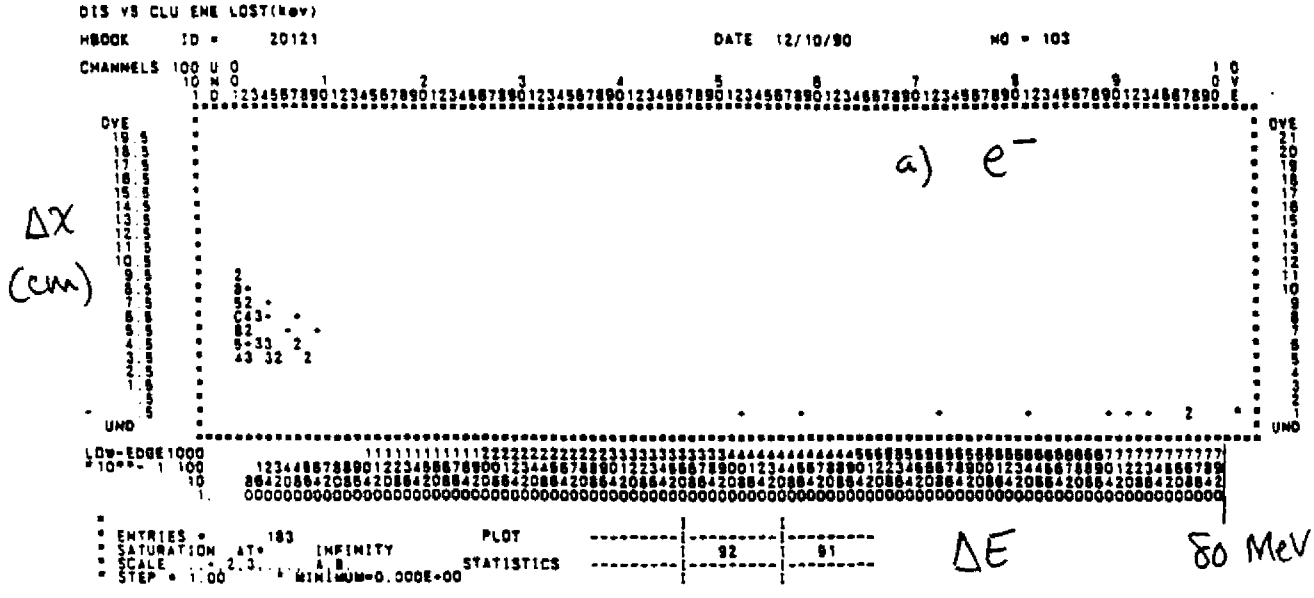

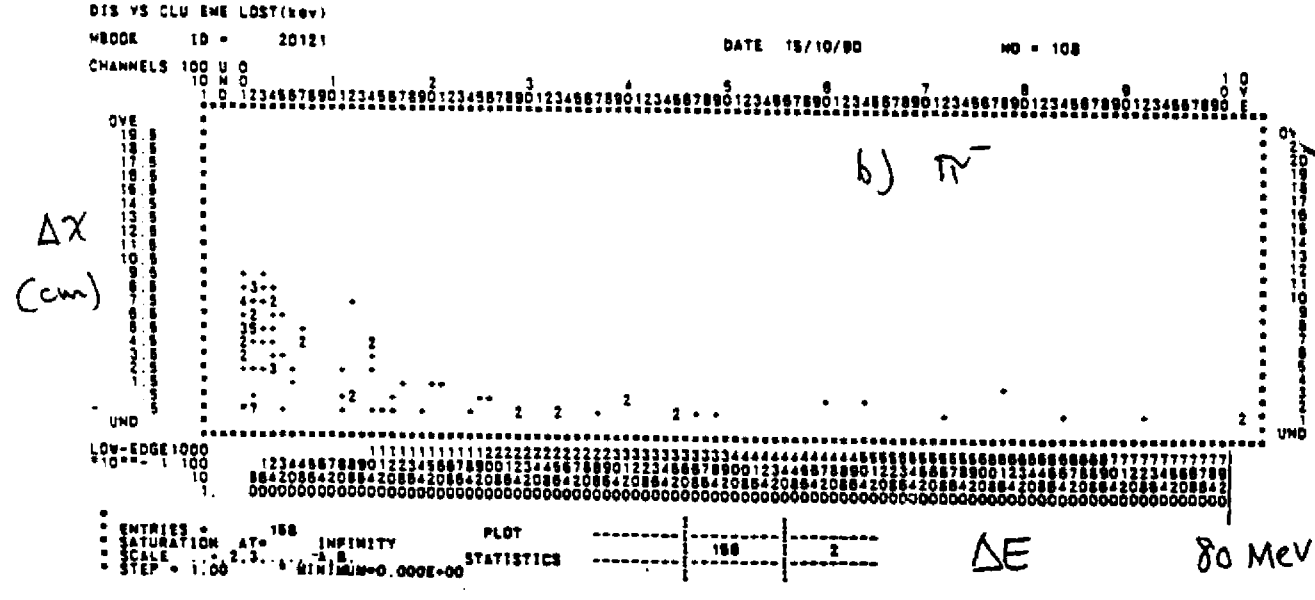

Figure 6.

Clusters in a SM detector at $|\eta| = 0$.

a) Electrons with E=40 GeV.

b) Charged pions with E=40 GeV.

The energy and position scales are different from those used for the PS data. Distances are in CM.

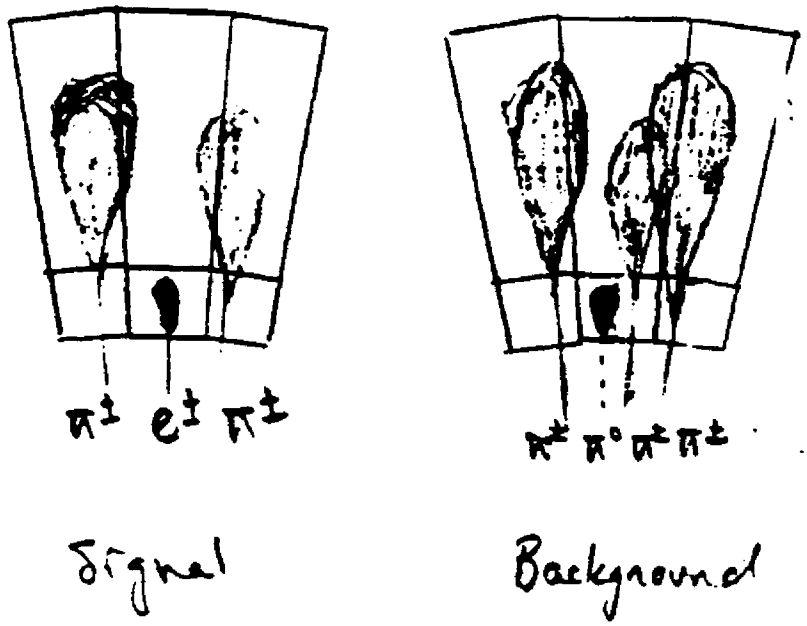

1) Ignore HAC - overlap from neighboring tower!
2) Require EM $E = P$ within $2\sigma(E-P)$
3) Require χ (PS/SM) = χ (tracking)
4) Assume background = $\pi^\pm \pi^0$
5) Assume most EM energy from π^0
6) Accept $e^\pm \pi^0$ overlap within $2\sigma(E-p)$
Best measurement from tracking.

Figure 7.
Signal and background in non-isolated electron studies, with the identification algorithm.

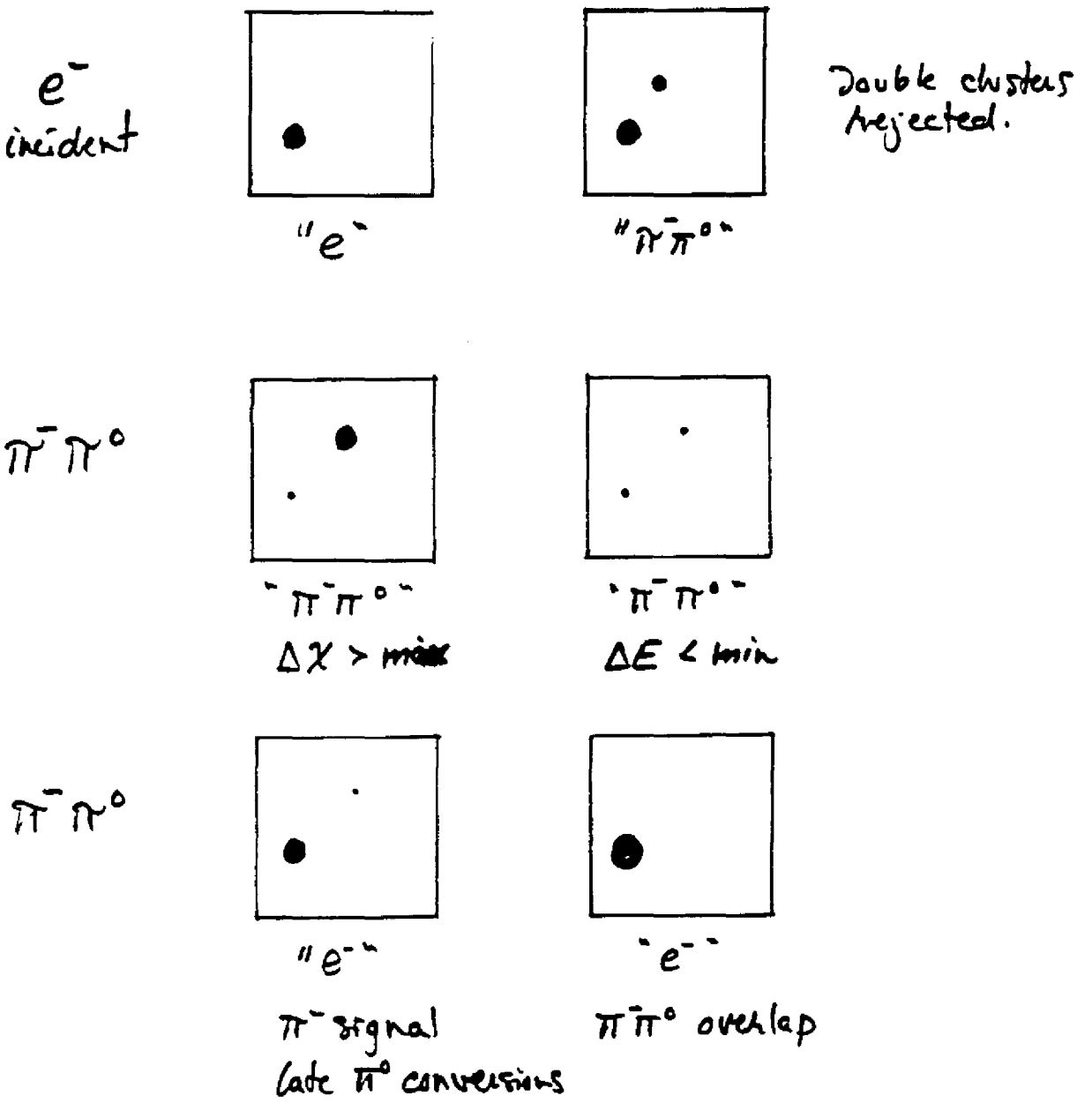

$$\text{Fake } e^- : \quad \epsilon_{\pi^-}(1-\epsilon_{\pi^0}) + \epsilon_{\pi^0}\frac{4\sigma_x \times 4\sigma_y}{\Delta X \cdot \Delta Y}$$

Figure 8.

Signal and background events in non-isolated electron studies. The actual source of the event is shown on the left. The interpretation is shown under the image.

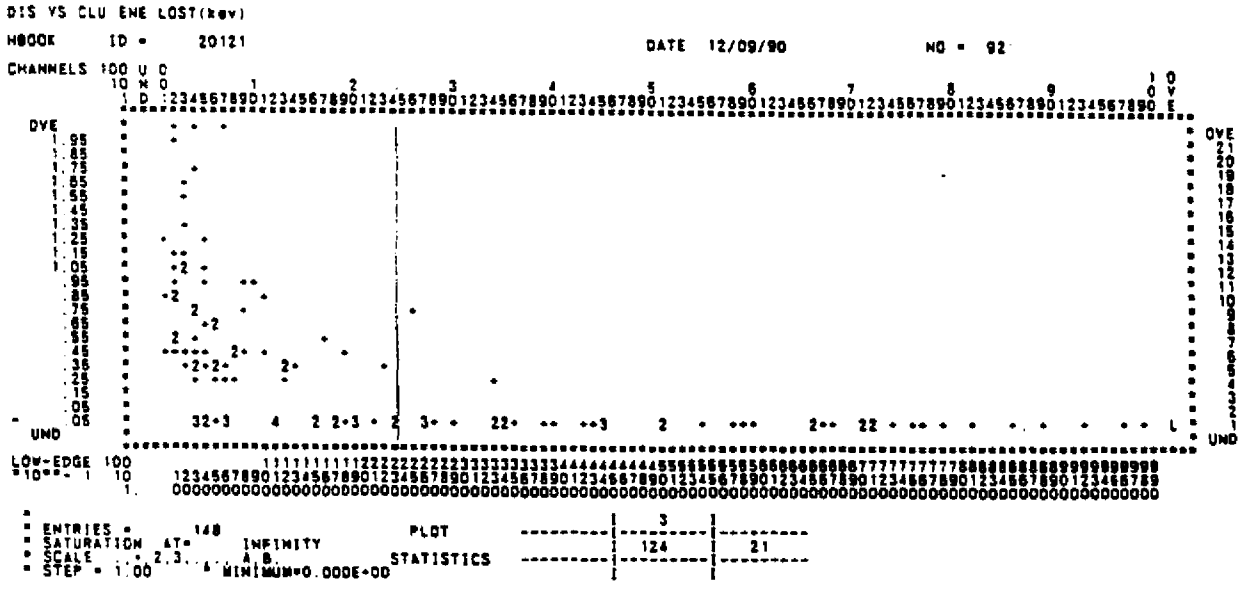

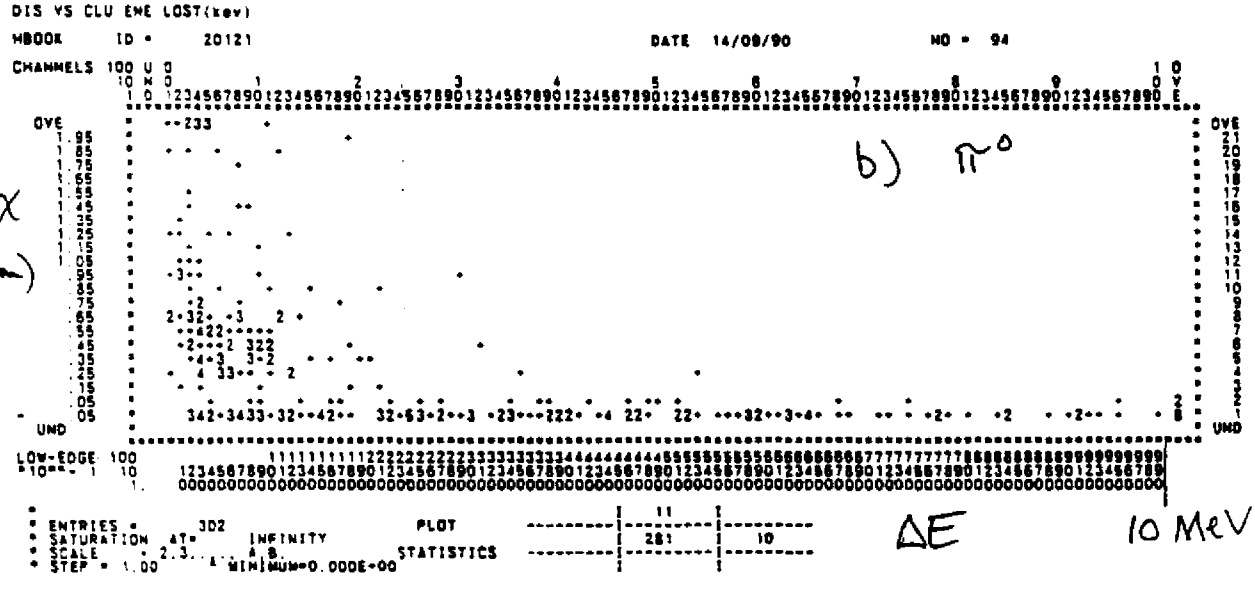

Figure 9.

Clusters in a PS detector at $|\eta| = 0$.

a) Gammas of E=40 GeV. 100 events.

b) Pi-zeros of E=40 GeV. 100 events.

The cluster energy is plotted against the distance from the incident gammas (in mm).

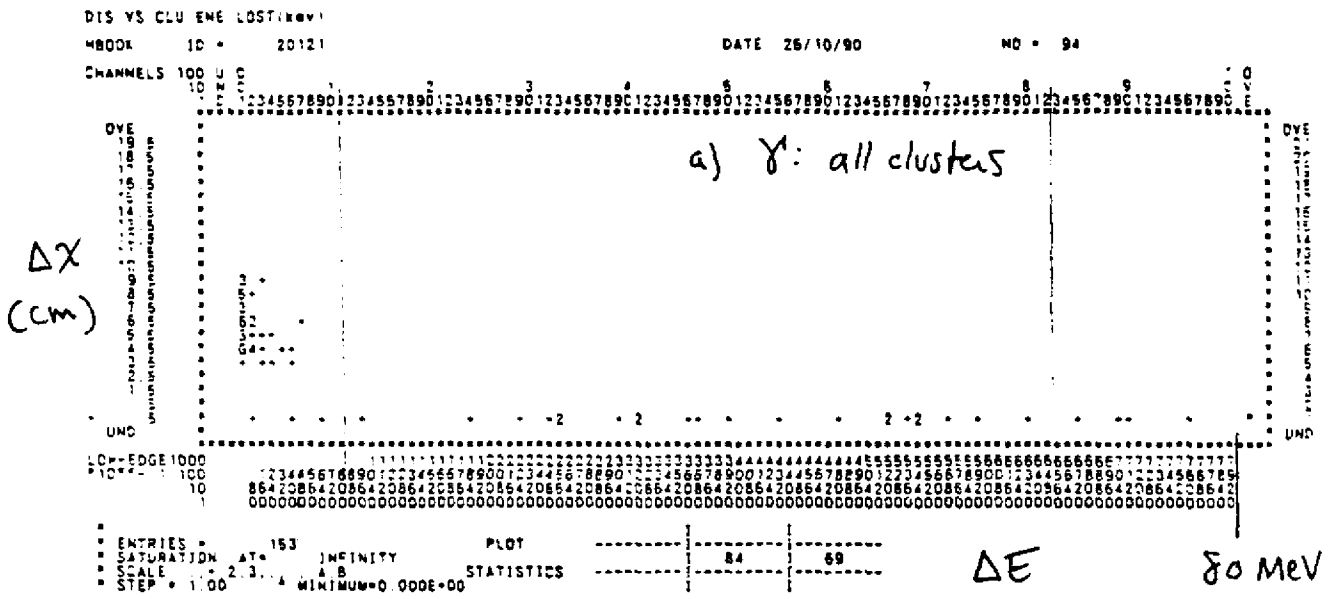

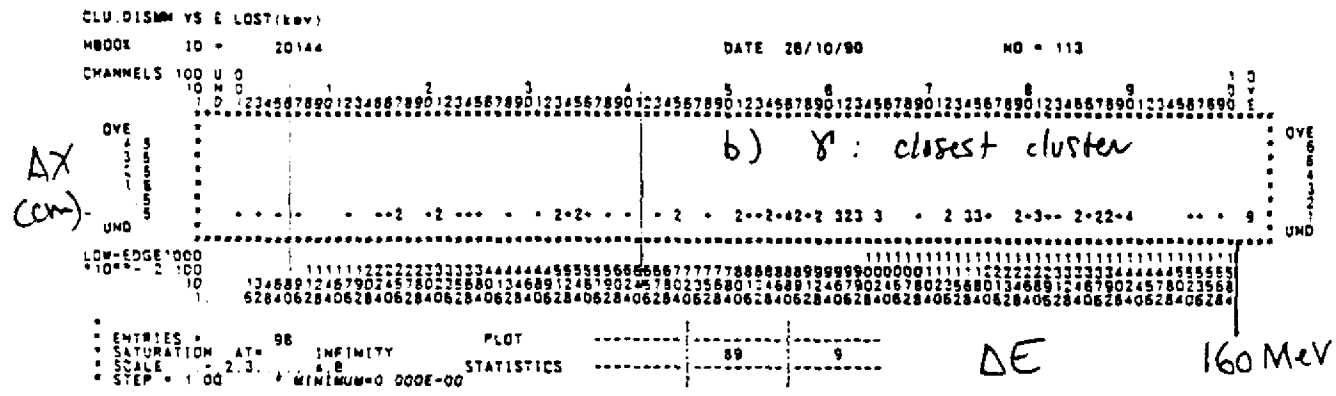

Figure 10.

Clusters from γ's in a SM detector at $|\eta| = 0$.

a) All clusters with the usual SM energy scale.

b) The closest cluster, with twice the energy scale.

100 events are shown with $E_\gamma = 40$ GeV.

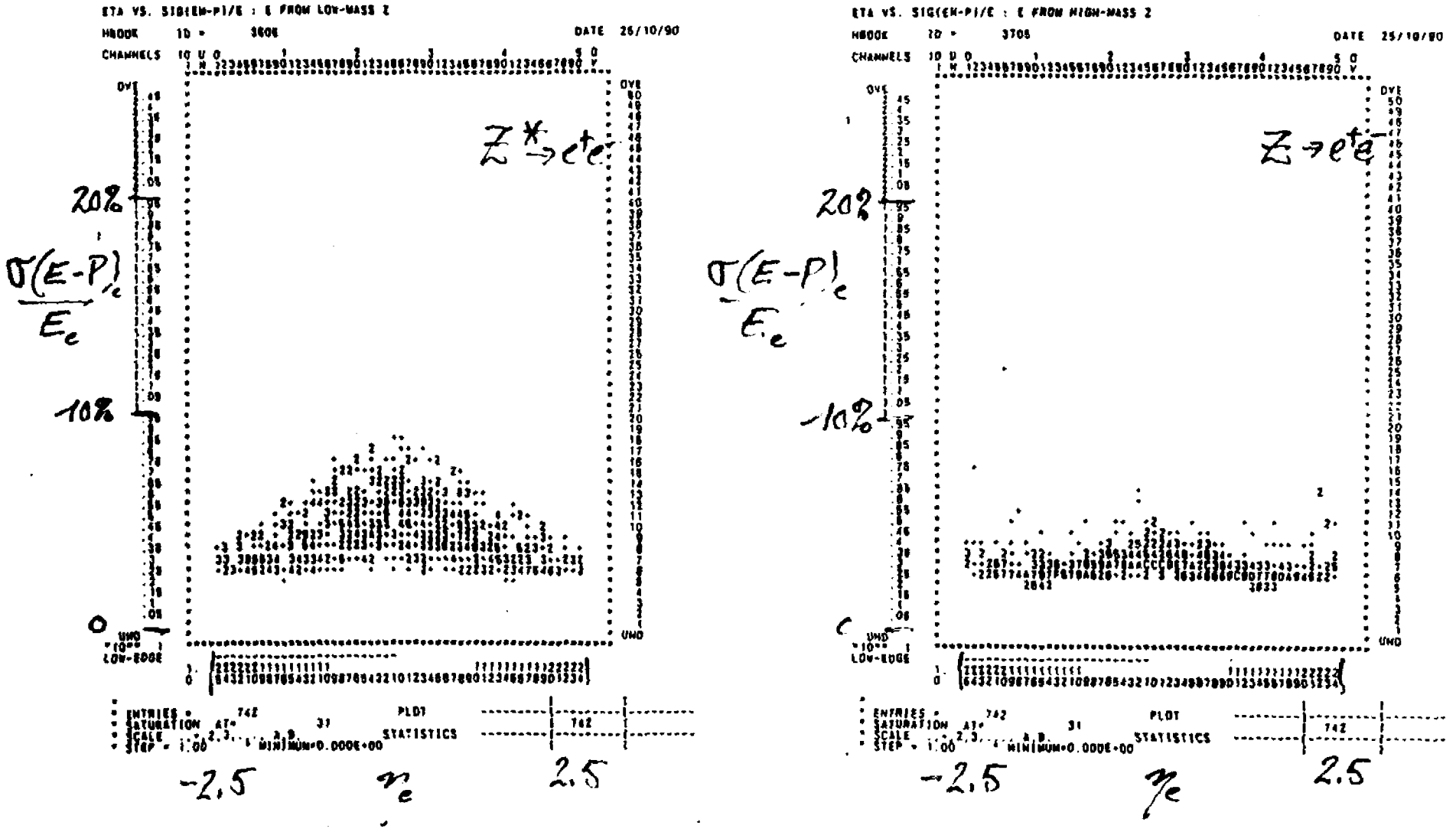

Figure 11.

Uncertainty in E/P vs. pseudorapidity (η) for electrons from $H \rightarrow Z Z^*$ with $M_H = 120$ GeV.

a) Electrons from $Z^* \rightarrow e^+e^-$.

b) Electrons from $Z \rightarrow e^+e^-$.

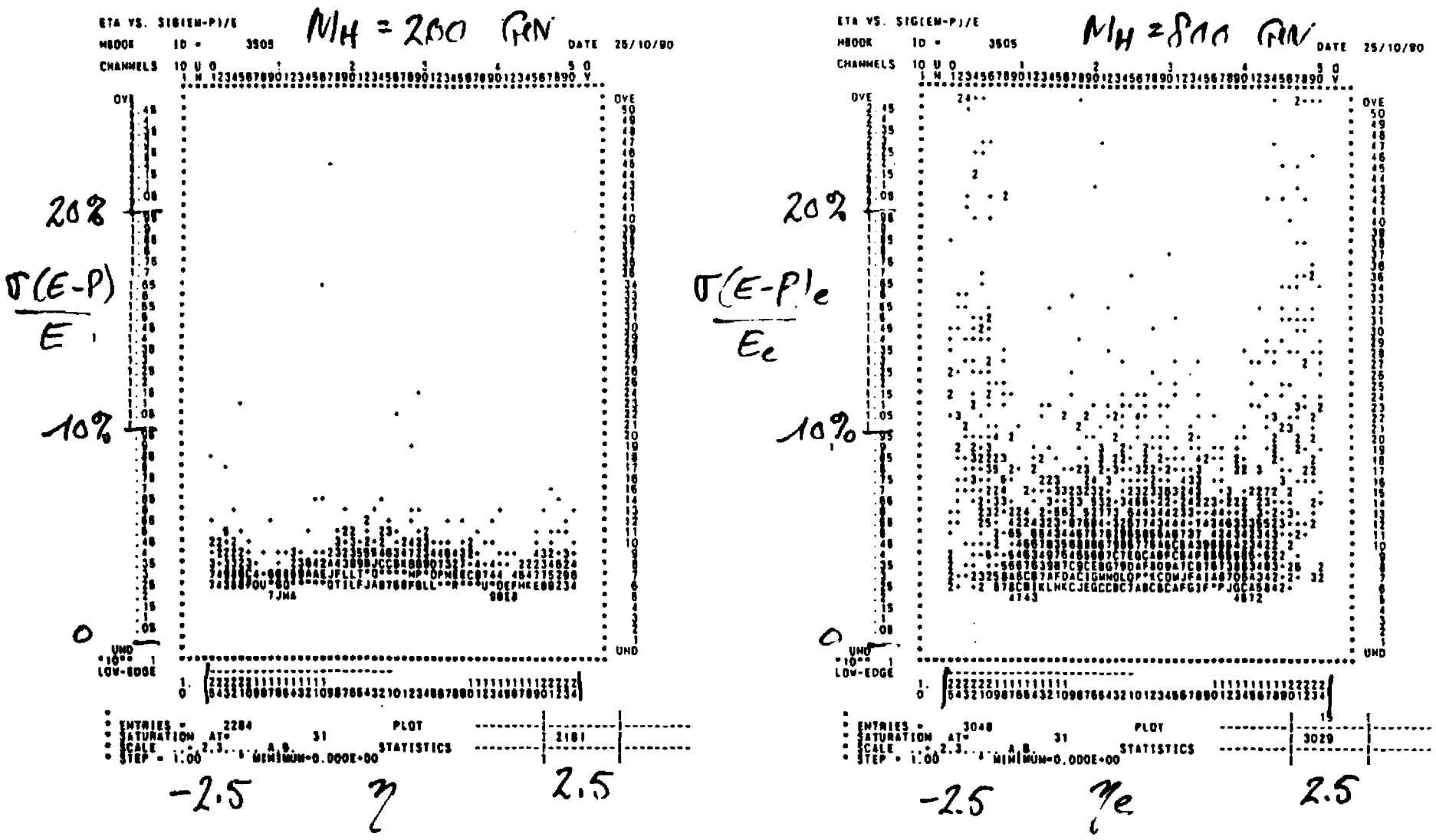

Figure 12.

Uncertainty in E/P vs. pseudorapidity for electrons from H→ Z Z.

a) M_H = 200 GeV.

b) M_H = 800 GeV.

$\bar{t} \rightarrow \bar{b} \rightarrow ce\nu$

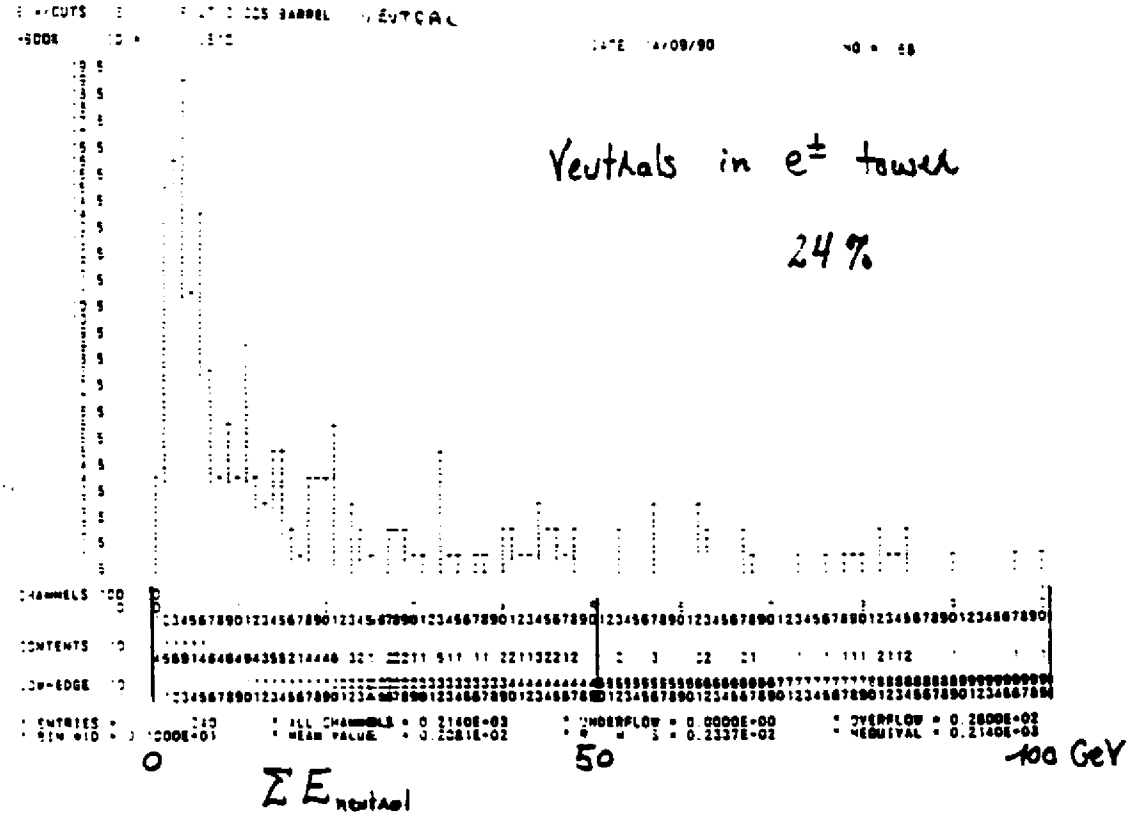

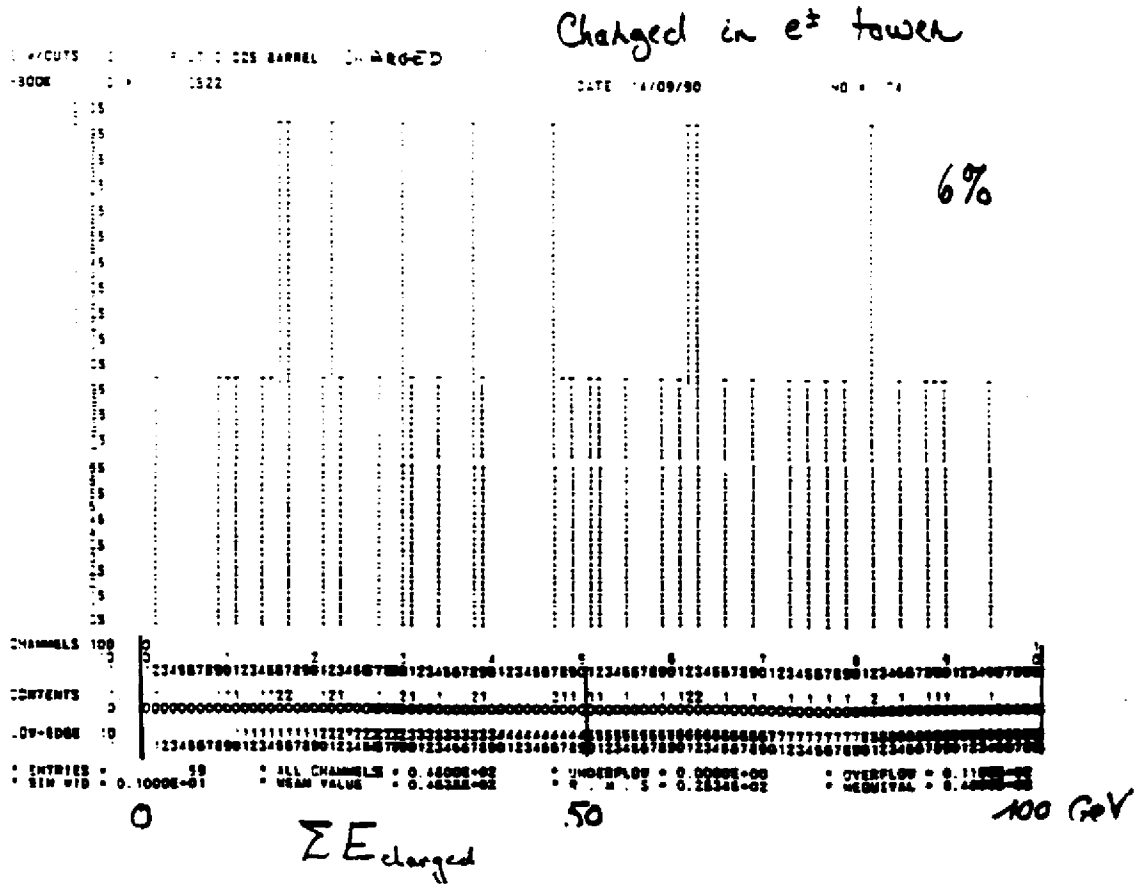

Figure 13.

Sum of a) neutral, b) charged energy in the same tower as the electron from $t \rightarrow b \rightarrow c\ e\ \nu$ decay.

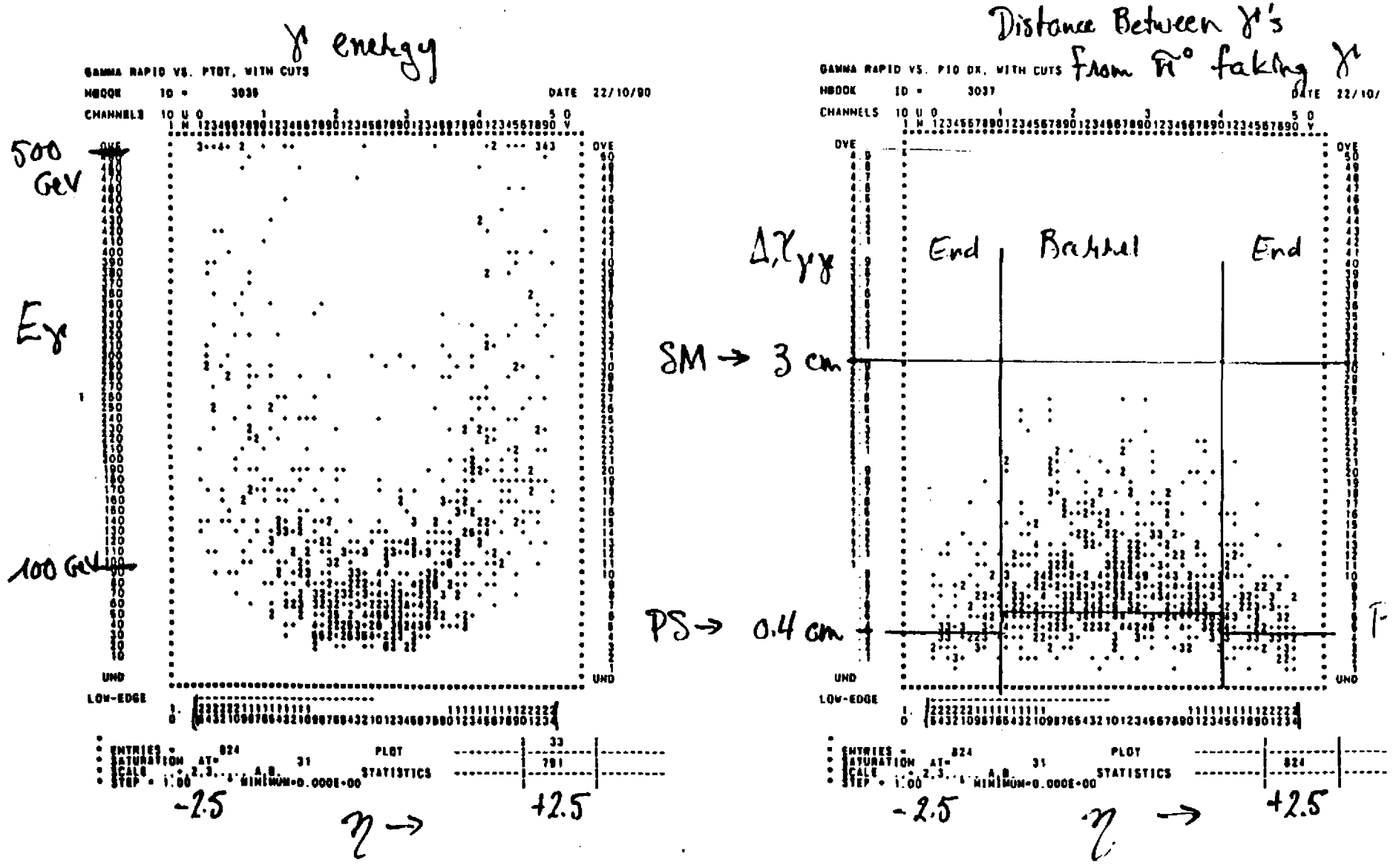

Figure 14.

W H $\rightarrow \ell \nu \gamma\gamma$ with $M_H = 120$ GeV.

a) γ energy vs. pseudorapidity (η) .

b) Minimum distance between γ's from π^0 decay faking an iso γ.

Figure 15.

General view of the scintillating fiber preshower detector. Clear fibers bring light from the barrel and end cap detectors to the photodetectors and front end electronics behind the calorimeter.

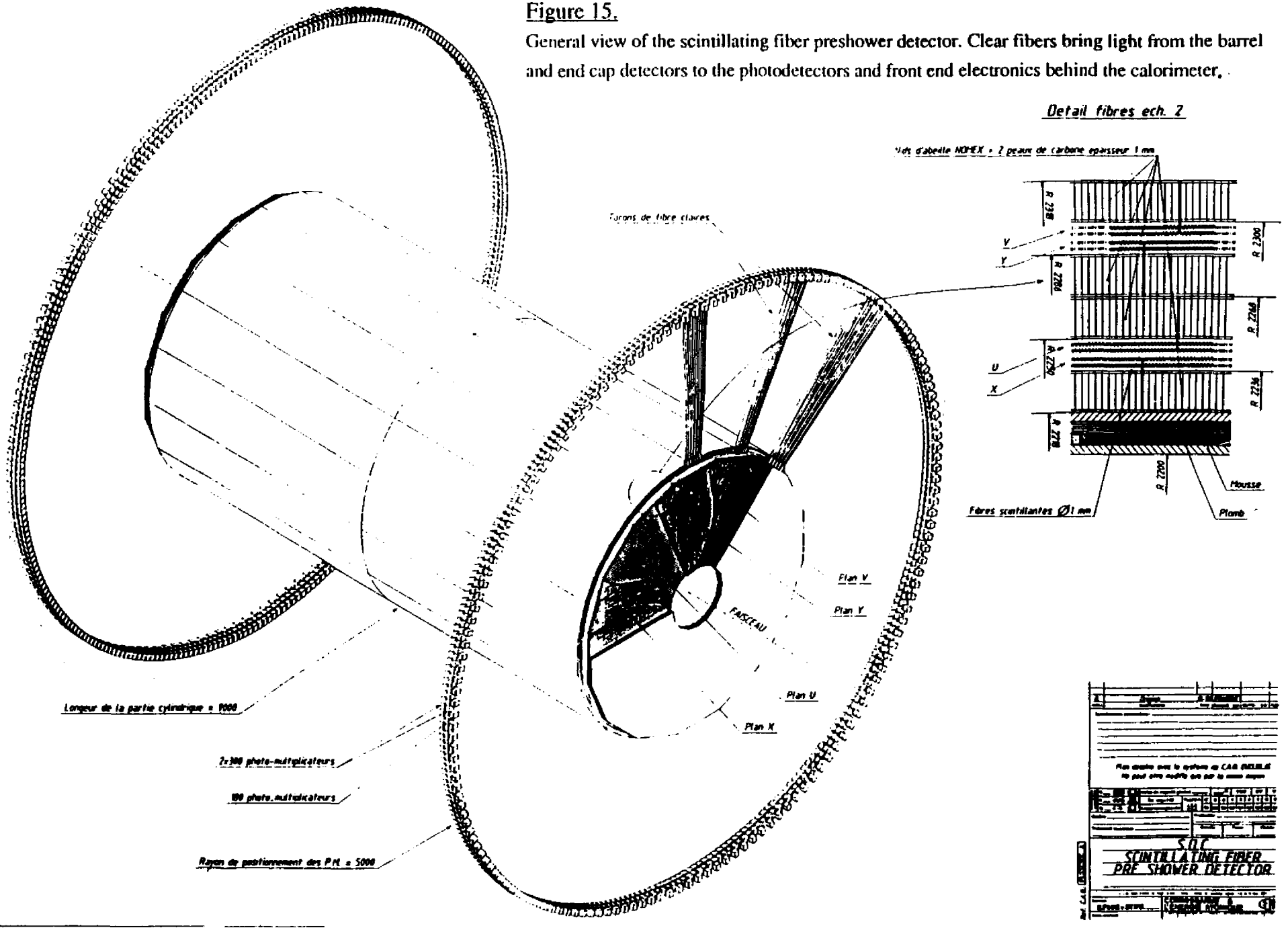

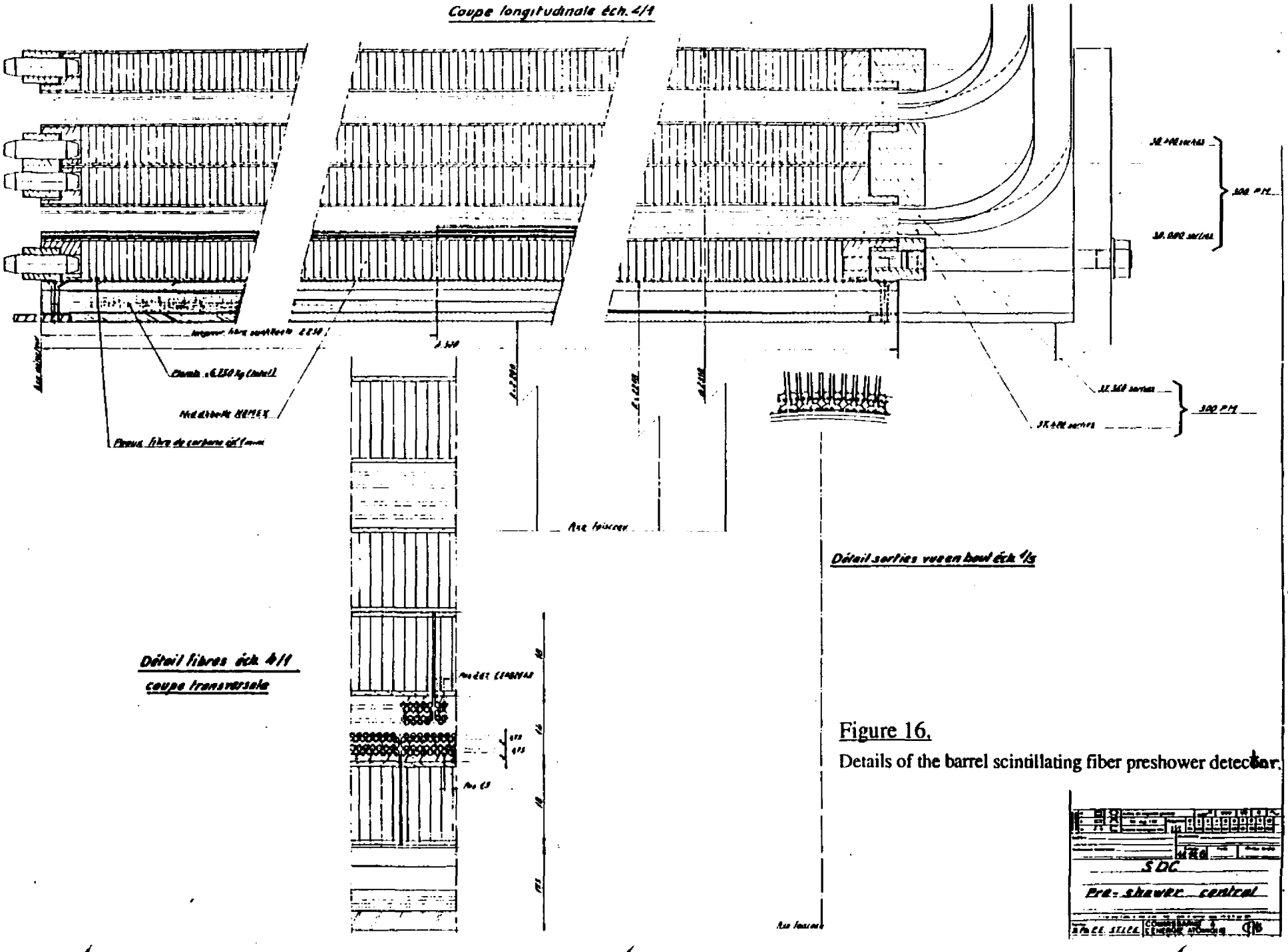

Figure 16.

Details of the barrel scintillating fiber preshower detector.

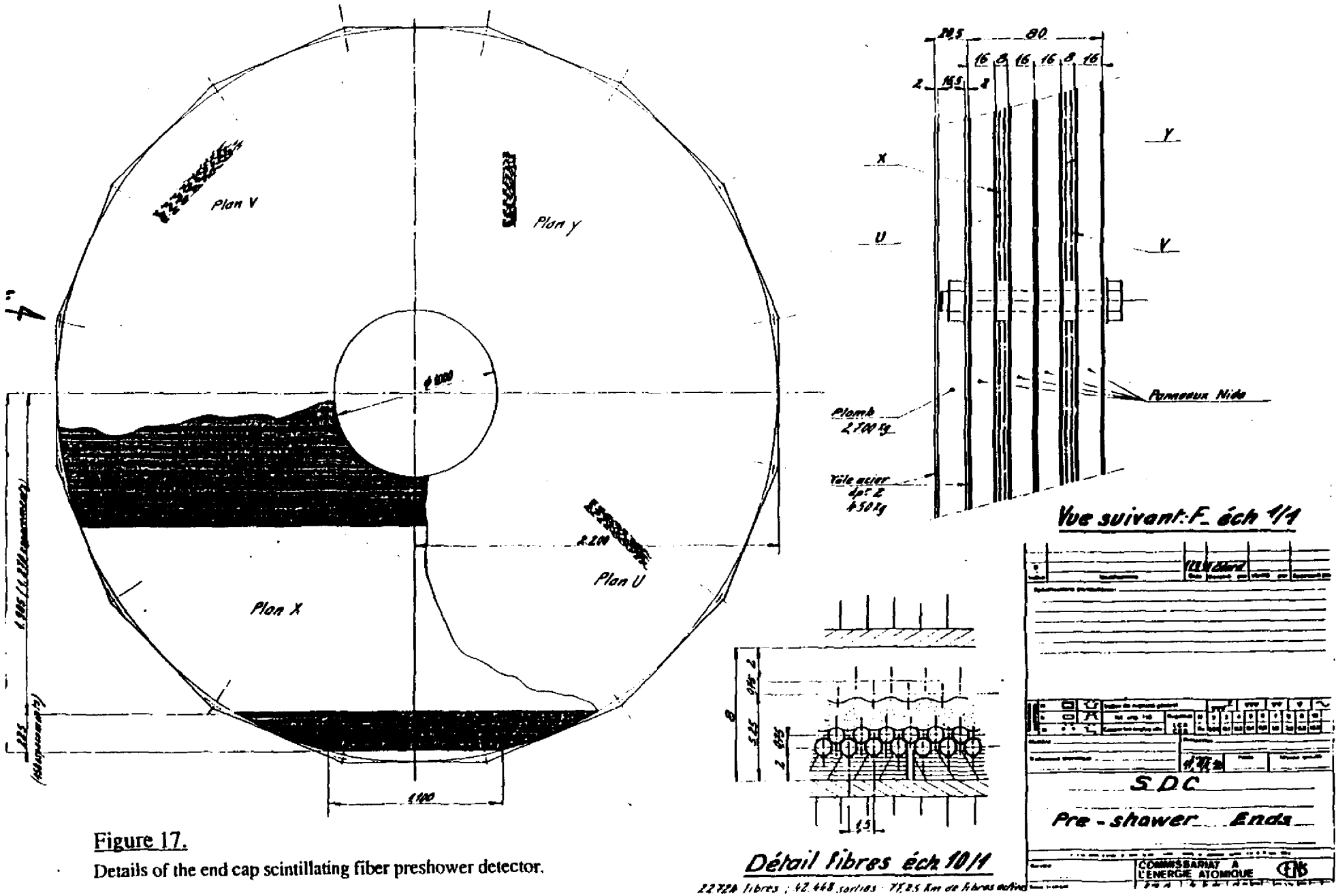

Figure 17.

Details of the end cap scintillating fiber preshower detector.